the MgO film was reduced below 3.6 monolayers (ML) and were almost closed for a thickness of 2.4 ML (Fig. 4). We observed essentially no variation in the XAS and XMCD spectra of Ho atoms with the number of MgO layers (fig. S5), hence the Ho ground state was unaffected by the MgO thickness. Thus, protection against first-order reversal is a necessary but not a sufficient condition to prevent magnetization reversal. To obtain long magnetic lifetimes in single atoms, an efficient decoupling from the electron and phonon bath is also required to ultimately suppress higher-order scattering processes that cannot be eliminated by symmetry. This result also suggests that long spin lifetimes are unlikely for single atoms in direct contact with a metal substrate.

The need of a decoupling layer to obtain long lifetimes is in stark contrast with the interpretation of STM experiments on Ho atoms on Pt(111), which reported telegraph noise in the differential conductance with characteristic times of up to 700 s at T = 0.7 K and zero field (*19*). This signal was interpreted as magnetic bistability and ascribed to a J_z = 8 ground state, as calculated by DFT, which would be protected by the C_{3v} symmetry of the adsorption site. However, XMCD measurements revealed that Ho atoms on Pt(111) have a ground state J_z = 6 that is incompatible with long spin lifetimes in a C_{3v}-symmetric crystal field (*27*). In addition, the magnetization curves at 2.5 K are fully reversible. According to these XMCD results, Ho/Pt(111) is a perfect paramagnet, as are all the other single atoms on surfaces previously reported. Moreover, subsequent STM experiments on the same system could reproduce neither telegraph noise nor spin excitations (*10*). Together with further STM observations on other 4f elements (*28*), this questions the interpretation of the results reported in (*19*) as magnetic bistability of Ho/Pt(111).

The relative simplicity of the Ho/MgO system, based on common physical deposition methods, as well as the planar geometry of the system opens the possibility of probing and manipulating the Ho spin and its environment in a controlled way. Using MgO as a decoupling layer could improve the magnetic stability not only of individual atoms but also of surface-supported molecular magnets, paving the road to scalable and robust nanoscale spintronic devices.

REFERENCES AND NOTES

1. R. Sessoli, D. Gatteschi, A. Caneschi, M. A. Novak, *Nature* **365**, 141–143 (1993).
2. N. Ishikawa, M. Sugita, T. Ishikawa, S. Y. Koshihara, Y. Kaizu, *J. Am. Chem. Soc.* **125**, 8694–8695 (2003).
3. M. Mannini *et al*., *Nature* **468**, 417–421 (2010).
4. J. M. Zadrozny *et al*., *Nat. Chem.* **5**, 577–581 (2013).
5. L. Ungur, J. J. Le Roy, I. Korobkov, M. Murugesu, L. F. Chibotaru, *Angew. Chem. Int. Ed.* **53**, 4413–4417 (2014).
6. J. D. Rinehart, M. Fang, W. J. Evans, J. R. Long, *J. Am. Chem. Soc.* **133**, 14236–14239 (2011).
7. S. Loth, S. Baumann, C. P. Lutz, D. M. Eigler, A. J. Heinrich, *Science* **335**, 196–199 (2012).
8. A. A. Khajetoorians *et al*., *Science* **339**, 55–59 (2013).
9. S. Yan, D.-J. Choi, J. A. J. Burgess, S. Rolf-Pissarczyk, S. Loth, *Nat. Nanotechnol.* **10**, 40–45 (2015).
10. M. Steinbrecher *et al*., *Nat. Commun.* **7**, 10454 (2016).
11. C. F. Hirjibehedin *et al*., *Science* **317**, 1199–1203 (2007).
12. F. Meier, L. Zhou, J. Wiebe, R. Wiesendanger, *Science* **320**, 82–86 (2008).
13. H. Brune, P. Gambardella, *Surf. Sci.* **603**, 1812–1830 (2009).
14. A. A. Khajetoorians *et al*., *Phys. Rev. Lett.* **106**, 037205 (2011).
15. F. Donati *et al*., *Phys. Rev. Lett.* **111**, 236801 (2013).
16. I. G. Rau *et al*., *Science* **344**, 988–992 (2014).
17. S. Baumann *et al*., *Science* **350**, 417–420 (2015).
18. P. Gambardella *et al*., *Science* **300**, 1130–1133 (2003).
19. T. Miyamachi *et al*., *Nature* **503**, 242–246 (2013).
20. C. Hübner, B. Baxevanis, A. A. Khajetoorians, D. Pfannkuche, *Phys. Rev. B* **90**, 155134 (2014).
21. P. Blaha, K. Schwarz, G. Madsen, D. Kvasnicka, J. Luitz, WIEN2k: An Augmented Plane Wave plus Local Orbitals Program for Calculating Crystal Properties (Karlheinz Schwarz, Techn. Universitat Wien, Austria, 2001).
22. Supplementary materials are available on *Science* Online.
23. M. Ganzhorn, S. Klyatskaya, M. Ruben, W. Wernsdorfer, *Nat. Nanotechnol.* **8**, 165–169 (2013).
24. J. Dreiser *et al*., *Appl. Phys. Lett.* **105**, 032411 (2014).
25. N. Ishikawa, M. Sugita, W. Wernsdorfer, *J. Am. Chem. Soc.* **127**, 3650–3651 (2005).
26. R. Giraud, W. Wernsdorfer, A. M. Tkachuk, D. Mailly, B. Barbara, *Phys. Rev. Lett.* **87**, 057203 (2001).
27. F. Donati *et al*., *Phys. Rev. Lett.* **113**, 237201 (2014).
28. D. Coffey *et al*., *Sci. Rep.* **5**, 13709 (2015).

ACKNOWLEDGMENTS

Funding from the Swiss National Science Foundation (grants 200021-153404, 200020-157081, 200021-146715, PZ00P2 142474, and IZ73Z0-152406) and the Swiss Competence Centre for Materials Science and Technology (CCMX) is gratefully acknowledged. L.P. was supported by an ETH Postdoctoral Fellowship (FEL-42 13-2). K.D. acknowledges support from the "EPFL Fellows" fellowship program cofunded by Marie Curie, FP7 grant agreement no. 291771. Z.S. was supported by the Serbian Ministry of Education and Science under grants ON171033 and ON171017. The DFT calculations were performed at the PARADOX-IV supercomputer at the Scientific Computing Laboratory (SCL) of the Institute of Physics Belgrade. The XMCD experiments were performed at the EPFL-PSI X-Treme beamline of the Swiss Light Source (SLS) and the ID32 beamline of the European Synchrotron Radiation Facility (ESRF). The authors declare that they have no competing financial interests.

SUPPLEMENTARY MATERIALS

www.sciencemag.org/content/352/6283/318/suppl/DC1
Materials and Methods
Figs. S1 to S9
Tables S1 to S3
References (*29*–*56*)

4 December 2015; accepted 8 March 2016
10.1126/science.aad9898

HYDROGEN BONDING

Nuclear quantum effects of hydrogen bonds probed by tip-enhanced inelastic electron tunneling

Jing Guo,[1]* Jing-Tao Lü,[2]* Yexin Feng,[1,3]* Ji Chen,[1] Jinbo Peng,[1] Zeren Lin,[1] Xiangzhi Meng,[1] Zhichang Wang,[1] Xin-Zheng Li,[4,5]† En-Ge Wang,[1,5]† Ying Jiang[1,5]†

We report the quantitative assessment of nuclear quantum effects on the strength of a single hydrogen bond formed at a water-salt interface, using tip-enhanced inelastic electron tunneling spectroscopy based on a scanning tunneling microscope. The inelastic scattering cross section was resonantly enhanced by "gating" the frontier orbitals of water via a chlorine-terminated tip, so the hydrogen-bonding strength can be determined with high accuracy from the red shift in the oxygen-hydrogen stretching frequency of water. Isotopic substitution experiments combined with quantum simulations reveal that the anharmonic quantum fluctuations of hydrogen nuclei weaken the weak hydrogen bonds and strengthen the relatively strong ones. However, this trend can be completely reversed when a hydrogen bond is strongly coupled to the polar atomic sites of the surface.

In terms of tunneling and zero-point motion, nuclear quantum effects (NQEs) play important roles in the structure, dynamics, and macroscopic properties of hydrogen-bonded (H-bonded) materials (*1*–*5*). Despite enormous theoretical efforts toward pursuing proper treatment of the nuclear motion at a quantum mechanical level (*5*–*9*), accurate and quantitative description of NQEs on the H-bonding interaction has proven to be experimentally challenging. Conventional methods for probing the NQEs are based on spectroscopic or diffraction techniques (*4*, *10*–*14*). However, those techniques have poor spatial resolution and only measure the average properties of many H bonds, which are susceptible to structural inhomogeneity and local environments. The spatial variation and interbond coupling of H bonds lead to spectral broadening that may easily smear out the subtle details of NQEs.

[1]International Center for Quantum Materials, School of Physics, Peking University, Beijing 100871, P. R. China. [2]School of Physics and Wuhan National High Magnetic Field Center, Huazhong University of Science and Technology, Wuhan 430074, P. R. China. [3]School of Physics and Electronics, Hunan University, Changsha 410082, P. R. China. [4]School of Physics, Peking University, Beijing 100871, P. R. China. [5]Collaborative Innovation Center of Quantum Matter, Beijing 100871, P. R. China.
*These authors contributed equally to this work. **†Corresponding author. E-mail: xzli@pku.edu.cn (X.-Z.L.); egwang@pku.edu.cn (E.-G.W.); yjiang@pku.edu.cn (Y.J.)**

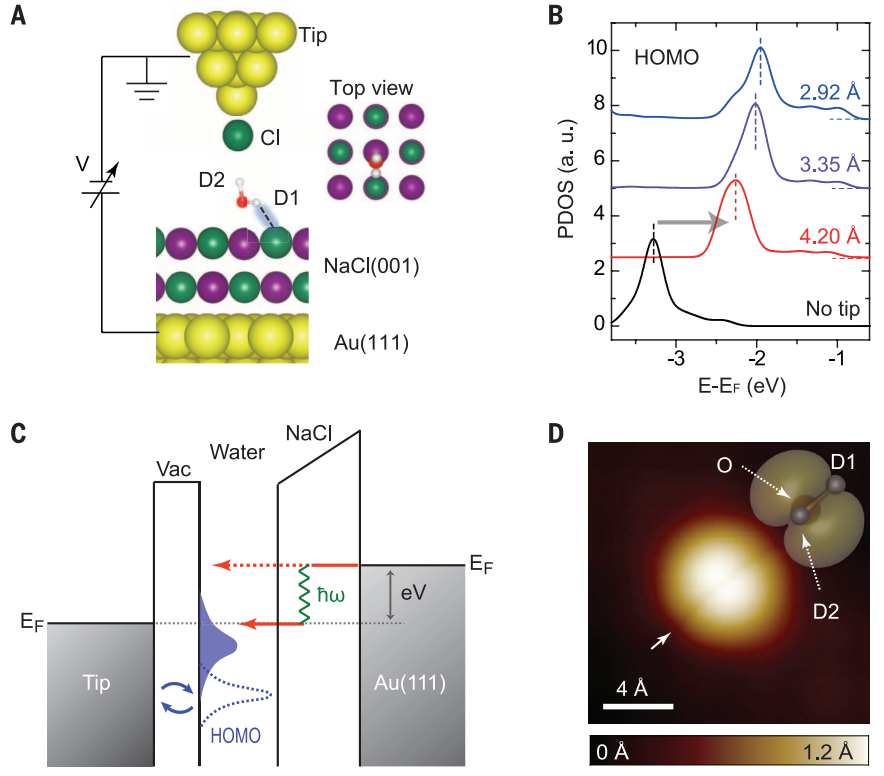

Fig. 1. Experimental setup and orbital gating. (**A**) Schematic of the experimental setup. One OD bond (D2) of the D_2O monomer is free and the other (D1) forms a H bond with Cl^- of NaCl (denoted by a dashed line). O, D, Au, Cl^-, and Na^+ are denoted by red, white, golden, green, and purple spheres, respectively. (**B**) Calculated HOMO states of the water molecule at different tip heights. Dashed lines denote the peak positions of the HOMO states; the arrow indicates the gating of the HOMO toward the Fermi level by the STM tip. *E*, energy; E_F, Fermi level; PDOS, projected density of states; a.u., arbitrary units. (**C**) Schematic of the tip-enhanced IET process. The tip-water coupling "gates" HOMO to the proximity of E_F, thus resonantly enhancing the cross section of the IET process. Vac, vacuum; $\hbar$, Planck's constant divided by 2π; ω; vibrational angular frequency. (**D**) STM topography of a D_2O monomer (V = 100 mV, I = 50 pA). The inset shows the calculated isosurface of charge density of the HOMO.

One promising technique to overcome these challenges is inelastic electron tunneling spectroscopy (IETS) based on a scanning tunneling microscope (STM), which combines sub-ångström spatial resolution and single-bond vibrational sensitivity (*15*–*18*). In a conventional IETS regime, the electron-vibration coupling is only a weak perturbation on the elastic scattering picture, leading to a very small cross section for vibrational excitation and extraordinarily weak IET signals (*19*, *20*). This limitation particularly affects closed-shell molecules such as water, whose frontier orbitals are located far away from the Fermi level (E_F) (*21*). Thus, it has been very difficult to obtain reliable vibrational spectroscopy of water with conventional IETS. To this end, we developed a tip-enhanced IETS technique to achieve a sufficiently high signal-to-noise ratio for water, which allowed us to quantitatively reveal the quantum component of the H bonds and the important role of the local environment in dictating the NQEs.

The STM-IETS experiments were performed on water monomers adsorbed on a Au-supported NaCl(001) bilayer (*22*) (fig. S1). The water is adsorbed on top of a Na^+ site in a "standing" configuration (*23*). One OD bond (D2) of a D_2O molecule dangles upward, and the other (D1) forms a H bond with the Cl^- of the NaCl surface (Fig. 1A). To enhance the IETS signals, we used a Cl-terminated STM tip to "gate" the highest occupied molecular orbital (HOMO) of water to the proximity of E_F via tuning tip-water coupling (Fig. 1B). Orbital gating with the Cl tip was highly selective and much more effective than gating with the bare tip, owing to the stronger coupling of the HOMO with the Cl p_z orbital (fig. S4). In such a near-resonance case, the HOMO is strongly coupled to the molecular

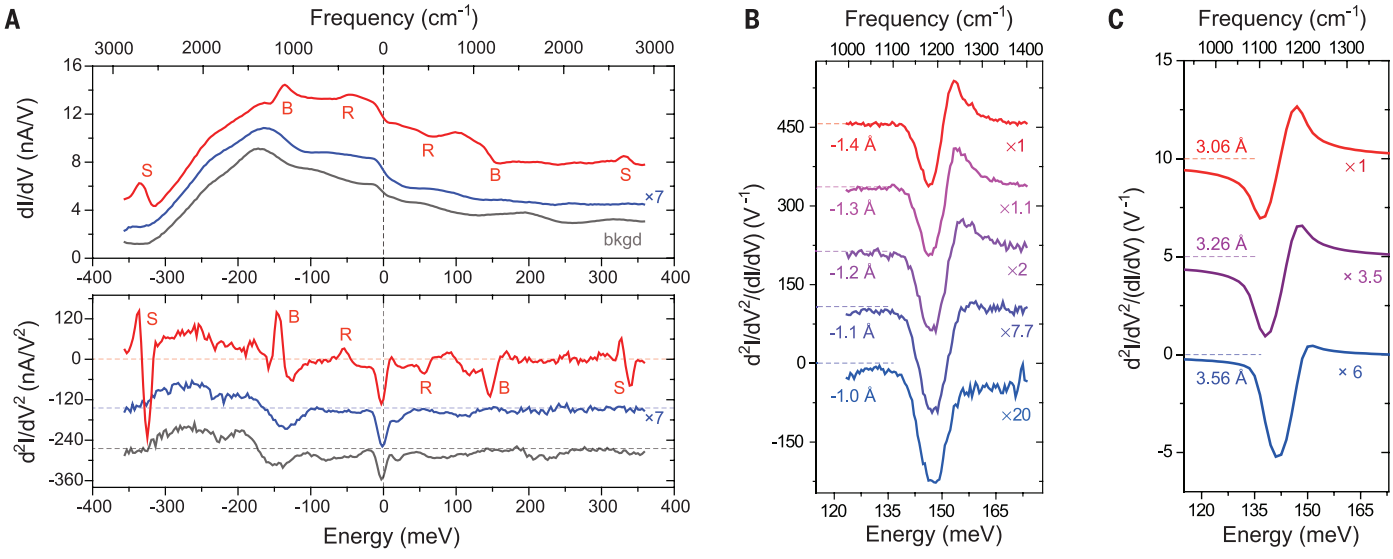

Fig. 2. Tip-enhanced IETS of a D_2O monomer. (**A**) dI/dV and d^2I/dV^2 spectra taken at different tip heights. Red (–1.2 Å) and blue (–0.4 Å) curves were taken on the D_2O monomer. Gray curves (–1.2 Å) were acquired on the NaCl surface (denoted as "bkgd"). The vibrational IET features are denoted as "R" (rotational), "B" (bending), and "S" (stretching). Dashed horizontal lines represent zero levels of the *y* axes for each curve. (**B** and **C**) Experimental (B) and calculated (C) d^2I/dV^2 spectra (normalized by dI/dV) of the bending mode as a function of tip height. For clarity, each curve is scaled properly to ensure the same magnitude. All tip heights in the experiment are referenced to the gap set with V = 100 mV and I = 50 pA. The tip height in (C) is defined in fig. S2.

vibrational modes ($\hbar\omega$, where $\hbar$ is Planck's constant h divided by 2π and ω is the vibrational angular frequency), resulting in a resonantly enhanced IET process (Fig. 1C) (*24*–*26*). The STM topography of the D_2O monomer near the zero bias exhibited a HOMO-like double-lobe structure with a nodal plane in between the lobes (Fig. 1D and fig. S4).

For typical tip-enhanced IETS of the D_2O monomer (Fig. 2A), the Cl tip was positioned slightly away from the nodal plane of the molecule (fig. S5). At a large tip-water separation, the spectra were featureless (blue), simply following the background (gray). Once the tip-water separation was decreased by ~0.8 Å (red), additional kinks arose in the dI/dV spectrum (I, current; V, voltage). In the corresponding d^2I/dV^2 curve, these kink features are further magnified as prominent peaks and dips that are point-symmetric with respect to the zero bias. Comparison with density functional theory (DFT) calculations allowed us to assign the spectral features ("R," "B," and "S") to the frustrated rotational, bending, and stretching modes, respectively (fig. S6).

High-resolution d^2I/dV^2 spectra of the bending mode (B) (Fig. 2B) show that as the tip height decreased, the normalized IETS intensity was enhanced by more than one order of magnitude, and the line shape changed from a symmetric dip to an asymmetric Fano-shaped feature (*25*). Such behavior was well reproduced by DFT-based transport calculations (Fig. 2C) (*22*), which revealed that the drastic increase of the spectral intensity mainly arose from the enhancement of the HOMO states near the bias window of IETS, whereas the symmetric-to-asymmetric line shape change arose from the competition between two high-order elastic channels controlled by the tip-water coupling (fig. S7). The resonantly enhanced IETS had a very high signal-to-noise ratio (up to 30% in relative conductance change), which is crucial for precisely determining the H-bonding strength.

The frequency shift of the stretching mode (S) is very sensitive to H-bonding strength (*27*, *28*). The adsorbed D_2O has two distinct S modes (denoted as D1 and D2 in Fig. 3A). The energy of D2 nearly coincides with that of the free OD stretching and thus should arise from the upright dangling OD bond (Fig. 1A). We attributed the other mode (D1), which was considerably red-shifted, to the downward OD H-bonded with the NaCl surface. For H_2O, only the red-shifted mode (H1) could be observed; the higher mode (H2) was too weak to produce any detectable signal (Fig. 3A). The spectral intensity of D2 was also much smaller than that of D1. Such a difference can be explained by considering the propensity rules (fig. S8) (*29*, *30*).

Notably, we could continuously modify the H-bonding strength by adjusting the tip height. As the tip height decreased, the water molecule was pushed closer to the substrate by the Pauli repulsion force, which led to a strengthening of the O–D···Cl H bond (fig. S9). Accordingly, the two-dimensional (2D) color map of our IETS results shows that both D1 and D2 shifted to lower energies as the tip height decreased (Fig. 3B). The D2 mode almost vanished around –1.36 Å (marked by two arrows), where the D1 mode underwent a symmetric-to-asymmetric line shape change. The red shifts of the D1 and D2 modes were independent of the bias polarity, thus excluding the origin of the electric field effect. Note that Chiang *et al.* recently observed the vibrational frequency shift of a CO molecule in the STM junction that was not the result of H-bond formation (*31*).

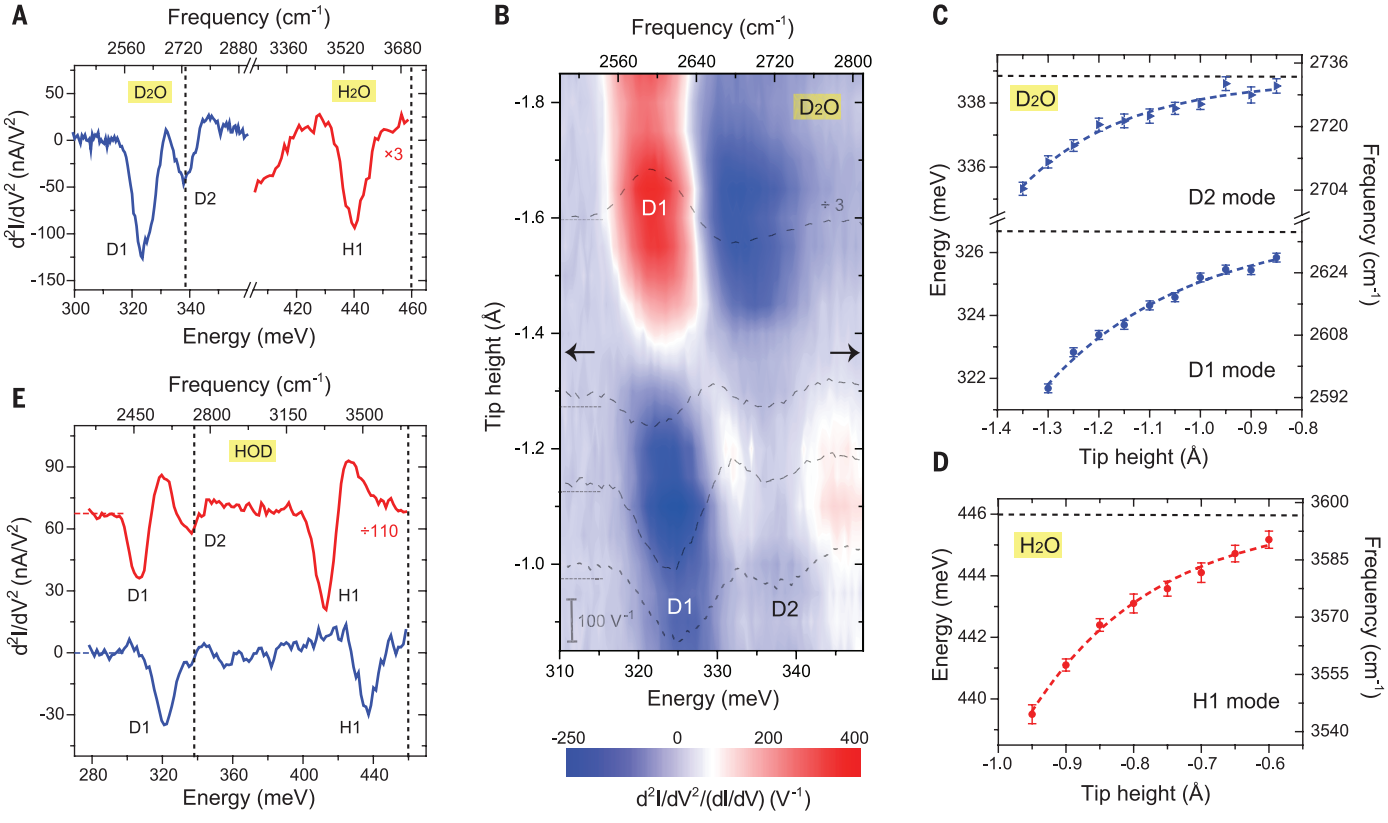

Fig. 3. Tuning the H-bonding strength with the Cl tip. (**A**) High-resolution IETS of D_2O (blue: –1 Å) and H_2O (red: –0.9 Å) monomers, focusing on the stretching modes (marked as D1, D2, and H1). Vertical dashed lines denote the vibrational energies of the free OD and OH stretching modes. (**B**) Two-dimensional (2D) IETS color map of the D_2O monomer as a function of tip height. Four representative IET spectra (dashed curves) at different tip heights are superimposed onto the map. Arrows denote the tip height of –1.36 Å, where the D2 mode nearly vanished and the D1 mode underwent a change in line shape from symmetric to asymmetric. (**C** and **D**) Energies of the D1, D2, and H1 modes as a function of tip height. Each data set can be nicely fitted to an inversed exponential decay. Horizontal dashed lines represent the asymptotic lines of those curves when extrapolated to infinite tip height. Error bars reflect the fitting error and the accuracy of the bias channel (~0.1 meV). (**E**) High-resolution IETS of a HOD monomer (blue: –1.4 Å, red: –2.3 Å).

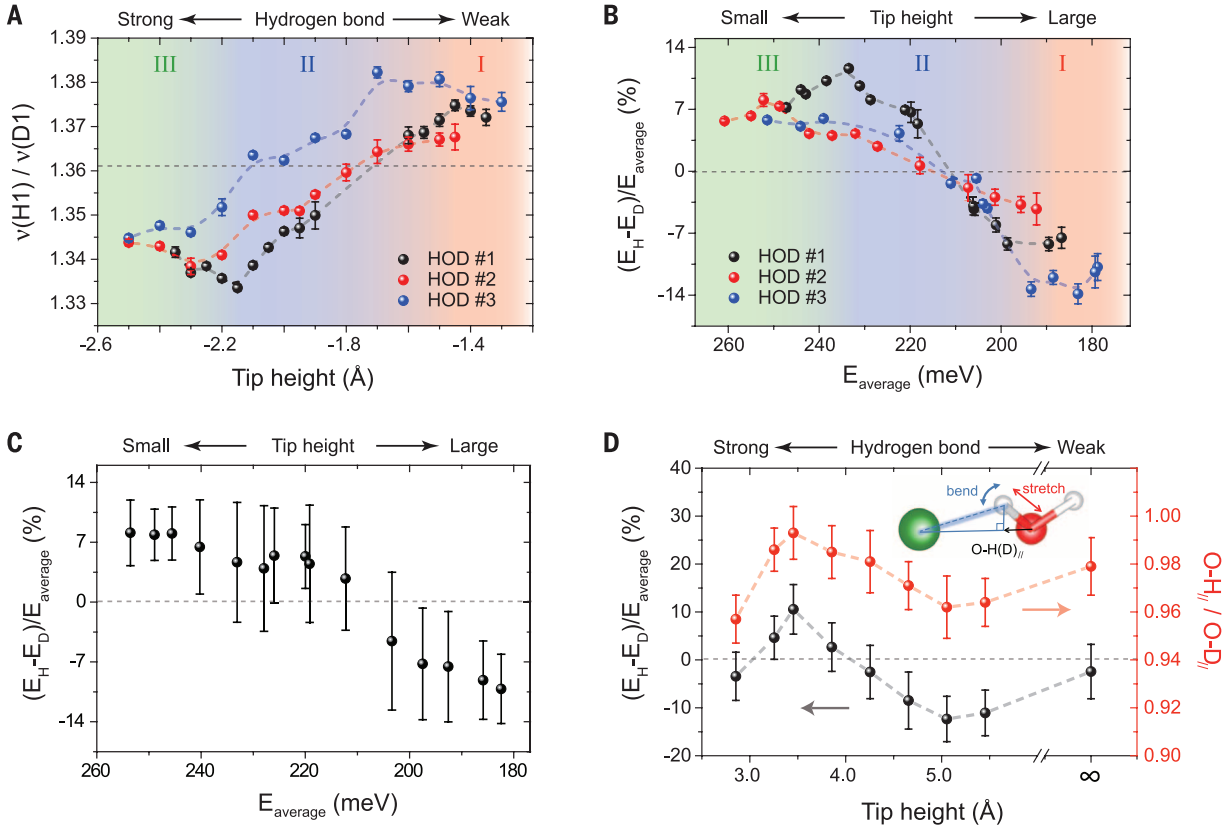

Fig. 4. Nuclear quantum effects on H-bonding strength of HOD monomers. (**A**) Ratio between the frequency (ν) of H1 and D1 as a function of tip height for three different HOD monomers. The ratio (1.361) between the frequency of the free OH and OD stretching modes is denoted by a horizontal dashed line. (**B**) Relative difference between H-bond energies of O–H···Cl (E_H) and O–D···Cl (E_D) as a function of their average [$E_{average} = (E_H + E_D)/2$]. Error bars in (A) and (B) were calculated by the uncertainty propagation formula from the errors of the D1 and H1 modes. (**C**) Same as (B), but the data were averaged for seven different HOD monomers. Error bars in (C) reflect the standard error. (**D**) Calculated H-bonding energy change upon isotope substitution (black) and the ratio between averaged projection of O–H and O–D covalent bonds along the intermolecular axis (red) as a function of tip height. The tip height is defined in fig. S2. The inset illustrates the geometry used for projecting the O–H(D) bond onto the intermolecular axis [O-H(D)$_{//}$]. Error bars in (D) reflect the statistical error in the PIMD simulations.

In Fig. 3, C and D, we plot the energies of the D1, D2, and H1 modes as a function of tip height, which can be fitted to inversed exponential decays (*22*). Extrapolating these curves to infinite tip height eliminated the influence of the STM tip. The resulting energy of D2 (338.7 ± 0.3 meV) is ~1 meV greater than that of the free OD stretching mode (338 meV). Such a blue shift may arise from the vibrational coupling between the D1 and D2 transition dipoles (fig. S6) (*32*). To minimize the contribution of vibrational coupling to the frequency shift, we switched to HOD monomers, in which OH and OD stretching are completely decoupled because of the large energy mismatch. Surprisingly, the OD and OH stretching modes were both red-shifted (blue curve in Fig. 3E), which suggests that they are both H-bonded. Upon decreasing the tip height, the free OD stretching mode (D2) emerged and coexisted with D1 (red). Thus, the HOD monomer must be rapidly flipping on the surface such that OH and OD form H bonds alternatively with the substrate (fig. S10).

This finding provides a rare opportunity to accurately quantify the NQEs on H-bonding strength by comparing the D1 and H1 modes in the same molecule. Figure 4A shows the ratio between the frequency of H1 and D1 (fig. S11) as a function of STM tip height for three different HOD monomers. As the tip approached the water molecule, this ratio decreased as a general trend. But at both large and small tip heights, distinct reversal behaviors appear (regions I and III). These curves differ from each other well beyond the experimental errors, which may arise from the influence of local environments created by the different condition of the tips and the inhomogeneity of the surface resulting from the Au substrate (fig. S1). In region II, these curves cross over the ratio of the free HOD monomer (1.361) (*33*), which is a clear indicator that NQEs affect the H-bonding interaction when isotope substitution occurs. We found that Stark shifts of the D1 and H1 modes are negligible because their dipole moments are almost orthogonal to the electric field of the STM tip (*34*).

To extract the impact of NQEs explicitly, we used an empirical relation to convert the red shifts of D1 and H1 into H-bonding energy (*22*, *27*). Figure 4B shows the relative H-bonding energy difference between H and D as a function of their average energies. In general, the NQEs weakened the weak H bonds and strengthened the relatively strong ones, but the impact of NQEs tended to diminish at the weak- and strong-bond limits (regions I and III). Figure 4C shows averaged data for seven different HOD monomers. Although the crossover still occurs, the turning points at both ends are smeared out after averaging. The quantum component of the H bond can account for up to 14% of the bond strength (Fig. 4B), which is much greater than the thermal energy contribution, even at room temperature.

To understand the behavior of NQEs, we carried out ab initio path integral molecular dynamics (PIMD) simulations (Fig. 4D and fig. S12) (*22*). The simulated results (black curve in Fig. 4D) are in excellent agreement with the experimental observations. To explore the physical basis for these changes, we defined a projection of the OH (OD) covalent bond length along the intermolecular axis of the H bonds (inset of Fig. 4D). The zero-point motion of O–H (O–D) stretching increases the projection, whereas that of H-bond bending decreases the projection, due to the anharmonic nature of the potentials. The ratio between the averaged O–H and O–D projections (red curve) correlates well with the bonding energy difference (black curve). A delicate interplay between covalent bond stretching and H-bond bending determines the bonding energy change upon isotope substitution.

The anharmonic quantum fluctuation of the stretching (bending) mode becomes more (less) pronounced as the H bond gets stronger (*9*), which accounts for the observed crossover behavior in region II. However, the reversal behaviors in regions I and III are not predicted by this simple theoretical picture. At the weak-bond limit (region I), the quantum contributions of these two modes both diminish quickly and tend to cancel each other, resulting in the fade-out of the energy difference. The turning point at the strong-bond limit (region III) is closely related to the unusual noncolinear geometry of the O–H···Cl H bond, which arises from the electric repulsive interaction between the H1 (D1) atom and the Na^+ cation of the NaCl surface (fig. S12). Such an interaction modifies the potential profile along the H-bond bending direction as the water molecule approaches the surface, so anharmonic H-bond bending is greatly enhanced and even dominates over O–H stretching, leading to the reversal behavior of NQEs for strong H bonds. This implies that the NQEs of a H bond are extremely sensitive to coupling with the local environment, which is, at present, inaccessible by macroscopic spectroscopic methods. Not only do these findings substantially advance our understanding of the quantum nature of H bonds, they also open up a new route for spectroscopic studies of H-bonded systems at the single-bond level.

REFERENCES AND NOTES

1. N. Greenwood, A. Earnshaw, *Chemistry of the Elements* (Butterworth Heinemann, 1997).
2. A. Hodgson, S. Haq, *Surf. Sci. Rep.* **64**, 381–451 (2009).
3. M. Benoit, D. Marx, M. Parrinello, *Nature* **392**, 258–261 (1998).
4. A. K. Soper, C. J. Benmore, *Phys. Rev. Lett.* **101**, 065502 (2008).
5. F. Paesani, G. A. Voth, *J. Phys. Chem. B* **113**, 5702–5719 (2009).
6. M. E. Tuckerman, D. Marx, M. L. Klein, M. Parrinello, *Science* **275**, 817–820 (1997).
7. G. A. Voth, D. Chandler, W. H. Miller, *J. Chem. Phys.* **91**, 7749–7760 (1989).
8. J. A. Morrone, R. Car, *Phys. Rev. Lett.* **101**, 017801 (2008).
9. X. Z. Li, B. Walker, A. Michaelides, *Proc. Natl. Acad. Sci. U.S.A.* **108**, 6369–6373 (2011).
10. D. F. Brougham, R. Caciuffo, A. J. Horsewill, *Nature* **397**, 241–243 (1999).
11. C. Andreani, D. Colognesi, J. Mayers, G. F. Reiter, R. Senesi, *Adv. Phys.* **54**, 377–469 (2005).
12. A. Pietropaolo *et al.*, *Phys. Rev. Lett.* **100**, 127802 (2008).
13. Y. Harada *et al.*, *Phys. Rev. Lett.* **111**, 193001 (2013).
14. Y. Nagata, R. E. Pool, E. H. G. Backus, M. Bonn, *Phys. Rev. Lett.* **109**, 226101 (2012).
15. B. C. Stipe, M. A. Rezaei, W. Ho, *Science* **280**, 1732–1735 (1998).
16. Y. Kim, T. Komeda, M. Kawai, *Phys. Rev. Lett.* **89**, 126104 (2002).
17. A. J. Heinrich, C. P. Lutz, J. A. Gupta, D. M. Eigler, *Science* **298**, 1381–1387 (2002).
18. H. Gawronski, M. Mehlhorn, K. Morgenstern, *Science* **319**, 930–933 (2008).
19. N. Lorente, M. Persson, *Phys. Rev. Lett.* **85**, 2997–3000 (2000).
20. M. Galperin, M. A. Ratner, A. Nitzan, A. Troisi, *Science* **319**, 1056–1060 (2008).
21. K. Morgenstern, J. Nieminen, *Phys. Rev. Lett.* **88**, 066102 (2002).
22. Supplementary materials are available on *Science* Online.
23. J. Guo *et al.*, *Nat. Mater.* **13**, 184–189 (2014).
24. B. N. J. Persson, A. Baratoff, *Phys. Rev. Lett.* **59**, 339–342 (1987).
25. M. Galperin, M. A. Ratner, A. Nitzan, *J. Chem. Phys.* **121**, 11965–11979 (2004).
26. H. Song *et al.*, *Nature* **462**, 1039–1043 (2009).
27. M. Rozenberg, A. Loewenschuss, Y. Marcus, *Phys. Chem. Chem. Phys.* **2**, 2699–2702 (2000).
28. T. Steiner, *Angew. Chem. Int. Ed.* **41**, 48–76 (2002).
29. N. Lorente, M. Persson, L. J. Lauhon, W. Ho, *Phys. Rev. Lett.* **86**, 2593–2596 (2001).
30. M. Ohara, Y. Kim, S. Yanagisawa, Y. Morikawa, M. Kawai, *Phys. Rev. Lett.* **100**, 136104 (2008).
31. C. L. Chiang, C. Xu, Z. Han, W. Ho, *Science* **344**, 885–888 (2014).
32. I. V. Stiopkin *et al.*, *Nature* **474**, 192–195 (2011).
33. A. V. Iogansen, *Spectrochim. Acta A* **55**, 1585–1612 (1999).
34. Y. Li *et al.*, *Nano Lett.* **16**, 1104–1109 (2016).

ACKNOWLEDGMENTS

This work was supported by the National Basic Research Programs of China under grant 2012CB921303 and the National Natural Science Foundation of China under grants 91321309, 11290162/A040106, 11304107, 61371015, 11422431, 11275008, 11274002, and 91021007. Y.J. acknowledges support from the National Program for Support of Top-Notch Young Professionals. We are grateful for the computational resources provided by the supercomputer TianHe-1A in Tianjin, China.

SUPPLEMENTARY MATERIALS

www.sciencemag.org/content/352/6283/321/suppl/DC1
Materials and Methods
Supplementary Text
Figs. S1 to S12
References (*35*–*50*)

6 January 2016; accepted 14 March 2016
10.1126/science.aaf2042

THERMODYNAMICS

A single-atom heat engine

Johannes Roßnagel,[1]* Samuel T. Dawkins,[1] Karl N. Tolazzi,[2] Obinna Abah,[3] Eric Lutz,[3] Ferdinand Schmidt-Kaler,[1] Kilian Singer[1,4]*

Heat engines convert thermal energy into mechanical work and generally involve a large number of particles. We report the experimental realization of a single-atom heat engine. An ion is confined in a linear Paul trap with tapered geometry and driven thermally by coupling it alternately to hot and cold reservoirs. The output power of the engine is used to drive a harmonic oscillation. From direct measurements of the ion dynamics, we were able to determine the thermodynamic cycles for various temperature differences of the reservoirs. We then used these cycles to evaluate the power P and efficiency η of the engine, obtaining values up to $P = 3.4 \times 10^{-22}$ joules per second and $\eta = 0.28\%$, consistent with analytical estimations. Our results demonstrate that thermal machines can be reduced to the limit of single atoms.

Heat engines, which convert thermal energy into mechanical work, have played a central role in society since the industrial revolution and are ubiquitous as generators of motion (*1*). The working fluid of a macroscopic engine typically contains on the order of 10^{24} particles. Experimental progress in the past decade has led to the miniaturization of thermal machines down to the microscale, using microelectromechanical (*2*), piezoresistive (*3*), and cold atom (*4*) systems, as well as single colloidal particles (*5*, *6*) and single molecules (*7*). In his 1959 talk "There is plenty of room at the bottom," Feynman envisioned tiny motors working at the single-atom level (*8*).

Here, we report the realization of a classical single-atom heat engine whose working agent is an ion held within a modified linear Paul trap. We use laser cooling and electric-field noise to engineer cold and hot reservoirs. To determine the temperature of the ion, we make use of fast thermometry methods, which make use of the Doppler broadening of optical resonances (*9*). The thermodynamic cycle of the engine is established for various temperature differences of the reservoirs, from which we deduce work and heat, and thus power output and efficiency. We additionally show that the work produced by the engine can be effectively stored and used to drive a harmonic oscillator against friction.

Trapped ions offer an exceptional degree of control in their preparation and manipulation, great precision in the measurement of their parameters (*10*, *11*), and the capability of coupling to engineered reservoirs (*12*, *13*). Hence, they provide an ideal setup for operating and characterizing a single-particle heat engine (*14*).

In our experiment, a single $^{40}Ca^+$ ion is trapped in a linear Paul trap with a funnel-shaped electrode geometry (Fig. 1A). The electrodes are driven symmetrically at a radio-frequency voltage of 830 V_{pp} at 21 MHz, resulting in a tapered harmonic pseudo-potential (Fig. 1B) of the form $U = (m/2)\sum_i \omega_i^2 i^2$ (*10*), where m is the atomic mass and $i \in \{x, y\}$ denotes the radial trap axes (Fig. 1A). The axial confinement is realized with constant voltages on the two end-cap electrodes, resulting in a trap frequency of $\omega_z/2\pi = 81$ kHz. The trap angle $\theta = 10°$ and the radial extent of the trap $r_0 = 1.1$ mm at $z = 0$ characterize the geometry of the funnel. The resulting radial trap frequencies $\omega_{x,y}$ decrease in the axial z-direction as

$$\omega_{x,y} = \frac{\omega_{0x,0y}}{\left(1 + \frac{z \tan\theta}{r_0}\right)^2} \quad (1)$$

The eigenfrequencies in the radial directions at the

[1]QUANTUM, Institut für Physik, Universität Mainz, D-55128 Mainz, Germany. [2]Max-Planck-Institut für Quantenoptik, D-85748 Garching, Germany. [3]Department of Physics, Friedrich-Alexander-Universität Erlangen-Nürnberg, D-91058 Erlangen, Germany. [4]Experimentalphysik I, Universität Kassel, D-34132 Kassel, Germany.
*Corresponding author. E-mail: j.rossnagel@uni-mainz.de (J.R.); ks@uni-kassel.de (K.S.)

Editor's Summary

Quantum effects in single hydrogen bonds

Hydrogen bonds are a combination of electrostatics with a nuclear quantum contribution arising from the light mass of hydrogen nuclei. However, the quantum states of hydrogen nuclei are extremely sensitive to coupling with local environments, and these effects are broadened and averaged with conventional spectroscopic or diffraction techniques. Guo *et al.* show that quantum effects change the strength of individual hydrogen bonds in water layers adsorbed on a salt surface. These effects are revealed in inelastic tunneling spectra obtained with a chlorine-terminated scanning tunneling microscope tip.

Science, this issue p. 321